JGR Solid Earth

RESEARCH ARTICLE
10.1029/2021JB022565

Key Points:

- Development of a new geomagnetic field model for the historical period from 1400 to 1900 CE
- The model evaluates and incorporates instrumental measurements and high-quality archeointensity data and bootstraps lower quality data
- Axial dipole intensity decreases between 1500 and 1600 CE and remains nearly constant between 1600 and 1900 CE

Supporting Information:

Supporting Information may be found in the online version of this article.

Correspondence to:

P. Arneitz,
patrick.arneitz@zamg.ac.at

Citation:

Arneitz, P., Leonhardt, R., Egli, R., & Fabian, K. (2021). Dipole and nondipole evolution of the historical geomagnetic field from instrumental, archeomagnetic, and volcanic data. *Journal of Geophysical Research: Solid Earth*, *126*, e2021JB022565. https://doi.org/10.1029/2021JB022565

Received 10 JUN 2021
Accepted 8 OCT 2021

Dipole and Nondipole Evolution of the Historical Geomagnetic Field From Instrumental, Archeomagnetic, and Volcanic Data

P. Arneitz[1], R. Leonhardt[1], R. Egli[1], and K. Fabian[2]

[1]ZAMG, Vienna, Austria, [2]NTNU, Trondheim, Norway

Abstract Although a large number of magnetic declination and inclination measurements are available for the historical period from 1400 to 1900 CE, even the evolution of the axial dipole moment, the most prominent quantity of the geomagnetic field, is highly disputed for this time interval. Here, a new iterative Bayesian spherical harmonic model is constructed that combines historical (direct) and archeomagnetic or volcanic (indirect) records to better constrain the geomagnetic field evolution over this historical epoch. The resulting geomagnetic field reconstruction (BIGMUDIh.1) benefits from recently published and revised data for critical periods and regions. The highly variable data uncertainties and qualities are tackled with a weighting and selection scheme. Model uncertainties are mainly controlled by selection criteria applied to indirect intensity records and are estimated using a bootstrapping approach. A major improvement with respect to the established historical model gufm1 consists in the incorporation of archeointensities, which enables a direct estimation of the axial dipole evolution prior to 1840 CE. BIGMUDIh.1 yields a ~2 μT (6%) decrease of the axial dipole component between 1500 and 1600 CE, followed by a relatively stable period until 1900 CE. Modeled declinations agree well with historical records and the gufm1 model derived from such records. Furthermore, the evolution of the South Atlantic Anomaly, driven by reverse flux patches (RFPs) at the core-mantle boundary, is outlined. Periods of accelerated movement of the northern magnetic dip pole appear to be connected to the formation and changes of RFPs in the Northern Hemisphere.

Plain Language Summary The geomagnetic field, generated in the Earth's outer core, is our primary shield against energetic cosmic particles, thus protecting living organisms and human infrastructures. The Earth's magnetic field has been systematically monitored during the last ~180 years, by a growing network of ground-based observatories, which has been complemented by satellite recordings during the last decades. These measurements revealed significant changes in the strength and directions of the geomagnetic field. A decrease of the global field (axial dipole) strength of ~7% has been determined since 1900 CE. This decline can be compared to more ancient geomagnetic variations derived from additional data sources. Man-made observations of the Earth's magnetic field date back to the 15th century and mainly provide information on the angle between the geographic and magnetic North direction (declination) derived from compass measurements for navigation purposes. Knowledge about the field strength prior to first man-made absolute intensity measurements in the 1830s can be gained from the laboratory analysis of rocks and archeological artifacts, which preserve the geomagnetic field over geological timescales. A combination of these different record types yields a decrease in the axial dipole strength of 6% during the 16th century followed by a nearly constant plateau until 1900 CE.

1. Introduction

Studying the past geomagnetic field variations is crucially important to understand the dynamics of planetary magnetic fields that shield the biosphere and technical infrastructure against energetic cosmic particles (e.g., Heirtzler et al., 2002) and the atmosphere against ablation by solar wind pressure (e.g., Moore & Horwitz, 2007). The study of ancient (axial) dipole moment fluctuations constrains the possible geodynamo mechanisms (e.g., Biggin et al., 2020) and radionuclide production within the Earth's atmosphere (e.g., Pavón-Carrasco et al., 2018). Despite recent efforts to provide continuous paleomagnetic field reconstructions for the last 100 Kyr (Panovska et al., 2018), the evolution of the axial dipole is still uncertain

even within the historical period from 1400 to 1900 CE (e.g., Finlay, 2008; Genevey et al., 2009; Gubbins et al., 2006; Poletti et al., 2018; Suttie et al., 2011; Troyano et al., 2021).

Since the introduction of direct absolute intensity measurements (Gauss, 1833), a significant decay of the axial dipole strength along with the increase of the South Atlantic Anomaly (SAA) has been observed. Reverse flux patches (RFPs) at the core-mantle boundary (CMB), such as those responsible for the SAA, have been proposed as a potential precursor of an upcoming field polarity reversal (e.g., Pavón-Carrasco & De Santis, 2016), which is also inferred from the analysis of dynamo models (Aubert et al., 2008; Wicht & Olson, 2004). Estimates of the geomagnetic field strength for times preceding systematic measurements solely rely on the analysis of the magnetization acquired by archeological artifacts and rocks (indirect records).

Different approaches have been used for reconstructing the geomagnetic field and/or the axial dipole coefficient g_1^0 within the historical period. In the spherical harmonic model gufm1 (Jackson et al., 2000), which is based only on historical data, g_1^0 was linearly extrapolated prior to 1840 CE, which was proposed by Barraclough (1974) due to the lack of field intensity records. Finlay (2008) also incorporated indirect intensity records and discussed problems of adequate weighting of archeointensities with respect to historical data. He concluded that the most probable model involves no change for g_1^0 between 1590 and 1840 CE, in line with the conclusions of Gubbins et al. (2006), who applied a linear fit through g_1^0 values derived from globally available archeointensity records at that time. More than 10 years later, a new combined model (BIGMUDI4k.1) based on the incorporation of direct and indirect records (Arneitz et al., 2019) suggested large variations of g_1^0 especially within the 18th century. In other studies, g_1^0 has been estimated from regional archeointensity data sets by recalibrating the axial dipole moments of gufm1 (Genevey et al., 2009; Troyano et al., 2021). In this way, a non-monotonic evolution of g_1^0—with a minimum in the second half of the 18th century—was reconstructed from the data sets of Uzbekistan and Western Eurasia.

Significant differences between dipole intensity reconstructions obtained with abovementioned approaches are not surprising, since each method has its own pitfalls and strengths. For instance, Troyano et al. (2021) used only highly consistent archeointensity records from two regions, derived from the Triaxe protocol (e.g., Gallet & Le Goff, 2006; Le Goff & Gallet, 2004), for determining a global quantity (i.e., g_1^0). Their approach reduces issues related to data heterogeneity and weighting, which represent the major problem of global (historical) field modeling (Arneitz et al., 2019; Finlay, 2008), at the cost of additional assumptions required to derive a global field parameter from data with poor spatial coverage.

In this study, a spherical harmonic modeling approach is presented in order to constrain the global geomagnetic field evolution throughout the historical period (BIGMUDIh.1). This approach closely follows that of Arneitz et al. (2019) and is based on the combination of direct and indirect input data. Additionally, a strong focus is set on data quality considerations derived from available studies on the reliability of archeointensity records with regard to laboratory protocols and data analysis (e.g., Arneitz, Egli, & Leonhardt, 2017; Paterson et al., 2014, 2017; Pavón-Carrasco et al., 2014; Suttie et al., 2011). For this purpose, the impact of different selection criteria is tested and a modified bootstrapping approach is developed in order to ensure reliable geomagnetic field reconstructions.

2. Data Set and Selection Criteria

The data set used to constrain the geomagnetic field evolution throughout the historical period (i.e., between 1400 and 1900 CE) is extracted from the updated HISTMAG database (Arneitz, Leonhardt, et al., 2017, https://cobs.zamg.ac.at/data/index.php/en/models-and-databases/histmag). Recent database updates include the addition of new indirect records from GEOMAGIA50.v3.4 database (Brown et al., 2015, https://geomagia.gfz-potsdam.de/, September 2020), which generally provides archeomagnetic and volcanic data based on thermoremanent magnetization (TRM) acquisition and from Schnepp et al. (2020). Furthermore, dates, geographical coordinates, and geomagnetic measurement values of ~1,000 historical records have been revised according to original sources and compilations (Dalrymple et al., 1778; de los Rios, 1621; Hansteen, 1819; Hescoatt, 1684; Knepp, 1683; Malaspina & Bustamante y Guerra, 1885; Sabine, 1840, 1843, 1846, 1849, 1875; Unknown, 1684; Van Bemmelen, 1899, see the HISTMAG website for details).

Table 1
Numbers of Direct and Indirect Records for Different Geomagnetic Field Components (n_F, n_D, and n_I) Available Between 1400 and 1900 CE[a]

Data set	n_F	n_D	n_I
Direct	9,601	144,931	14,861
Indirect D_{LQC}	1,043	757	1,749
Indirect D_{MQC}	370	757	1,749
Indirect D_{HQC}	200	757	1,749

[a]Different archeointensity selection criteria have been applied to the indirect data sets D_{LQC}, D_{MQC}, and D_{HQC}, respectively (see text for details).

Unlike the construction of BIGMUDI4k.1, where several archeomagnetic subsets have been neglected, only indirect records with purely archeomagnetically derived datings have been fundamentally excluded from BIGMUDIh.1. Selection of historical data sets corresponds to the procedure used for BIGMUDI4k.1 (see Arneitz et al., 2019, for details). The final data set is dominated by historical declination records (Figure S1 in Supporting Information S1 and Table 1). While only a few direct field observations are available for the 15th century (e.g., Korte et al., 2009), the number of such records significantly increases during the following centuries (Figure S1a in Supporting Information S1), mainly due to measurements performed during ship voyages (Jonkers et al., 2003). Indirect records are evenly distributed over the modeling period considered here; however, most of them are concentrated in the Northern Hemisphere (Figure S1b in Supporting Information S1). Archeomagnetic records are essential to constrain the geomagnetic field evolution prior to the advent of regular historical measurements, i.e., prior to 1830s CE with respect to field intensity and within the 15th and 16th centuries in terms of field directions.

Different data selection and weighting approaches are currently under discussion, with the scope of reducing or eliminating the effects of potentially biased indirect records (e.g., Arneitz, Egli, & Leonhardt, 2017; Pavón-Carrasco et al., 2014). Recently, Campuzano et al. (2019) found an optimum weighting factor of 10 for the high-quality archeomagnetic records with respect to other indirect data. Instead of using (arbitrary) weighting factors, archeointensity records are selected here on the basis of systematic errors that might be associated with certain laboratory protocols (e.g., lack of cooling rate or anisotropy corrections). Thresholds for statistical data uncertainties are not applied, because they deal with random errors already considered in the weighting scheme. Moreover, statistical uncertainties of field and age estimates are incorporated in the bootstrapping approach described in Section 3.2. Chosen selection criteria yield three data sets D_{LQC}, D_{MQC}, and D_{HQC} with low-, medium-, and high-quality criteria, respectively (see Figure 1, Table 1, and Data Set S1).

Data set D_{LQC} ($n = 1043$) includes all archeomagnetic records with no selection being applied. Archeointensities obtained with the original Thellier method (Thellier & Thellier, 1959) and its modified versions along with pTRM checks are often considered as highly reliable (e.g., Campuzano et al., 2019), as also confirmed by a recent statistical analysis (Arneitz, Egli, & Leonhardt, 2017). Archeointensity records fulfilling these requirements are compiled in data set D_{MQC} ($n = 370$). Stricter additional selection criteria that include the correction of effects associated with thermoremanent anisotropy and cooling rate dependence are applied for D_{HQC} ($n = 200$). The cooling rate selection criterion is applied only to archeomagnetic records, since most fired clays contain abundant fine-grained iron oxides that have a strong cooling rate dependence, but not to volcanic materials, which are dominated by large (i.e., pseudo-single- and multidomain) remanence carriers for which no significant cooling rate dependence is expected (e.g., Ferk et al., 2014). Some

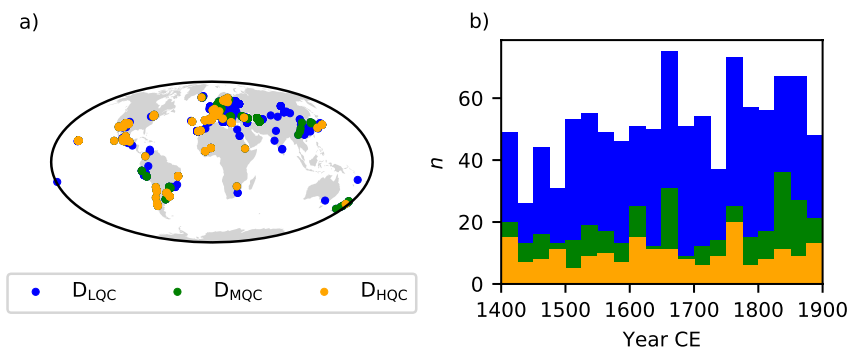

Figure 1. Geographical (a) and temporal (b) distribution of three data sets obtained with increasingly selective quality criteria, from D_{LQC} (low-quality criteria) to D_{HQC} (high-quality criteria). Note that D_{HQC} is a subset of D_{MQC}, which is in turn a subset of D_{LQC} (see text for details).

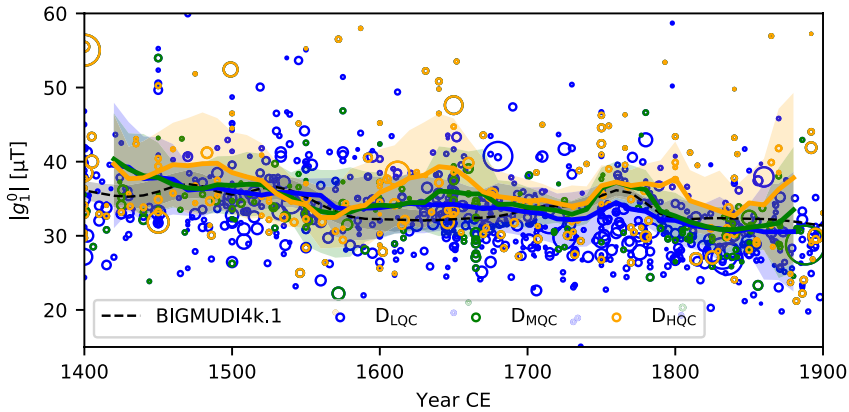

Figure 2. Absolute values of axial dipole coefficients $|g_1^0|$ obtained from individual records of the three archeointensity data sets D_{LQC}, D_{MQC}, and D_{HQC} (circles with size inversely proportional to the record uncertainty) and the corresponding 40-year weighted running averages (lines) with bootstrapping uncertainties (shaded bands). The evolution of g_1^0 predicted by BIGMUDI4k.1 is shown by the black-dashed line.

archeological materials (e.g., pottery and ceramics) are often affected by a strong thermoremanence anisotropy; therefore, only archeomagnetic data from such materials that have been corrected for anisotropy effects are selected in D_{HQC}. In contrast to Campuzano et al. (2019), who only accepted anisotropy corrections based on the TRM anisotropy tensor (Veitch et al., 1984), we accept all available anisotropy correction techniques. This approach is justified by the fact that, for example, anisotropy measurements of anhysteretic and isothermal remanent magnetization are often reported as an appropriate TRM substitute (Tema, 2009 and references therein).

Even though the number of indirect intensity records considerably decreases to about 35% and 19% for D_{MQC} and D_{HQC}, respectively, due to the application of abovementioned selection criteria, a widely uniform temporal coverage for all three data sets is maintained (Figure 1b). Nevertheless, high-quality data (from D_{HQC}) are very sparse, especially in the Eastern Hemisphere (Figure 1a).

The effect of data selection on geomagnetic field reconstructions is first tested on the basis of reconstructed global field strength over the modeling period (Figure 2). For this purpose, axial dipole coefficients $g_1^0 = F(1 + 3(\cos\theta)^2)^{-1/2}$ have been estimated from individual archeointensity values F and their geographic colatitude θ. Ten thousand bootstrap simulations have been generated with random variations of nominal intensity and age uncertainties assuming Gaussian and uniform error distributions, respectively. Default $\delta F = 5.7$ μT and $\delta t \pm 40$ yrs errors have been assigned to records lacking nominal uncertainty estimates based on Arneitz, Egli, and Leonhardt (2017) and on the median age uncertainty of all archeomagnetic records, respectively. Running 40-year weighted means in 10-year steps have been calculated for each bootstrap, and the resulting ensembles averaged to produce a continuous mean record.

Several differences can be seen in the evolution of $|g_1^0|$ estimates derived from the three data sets. Data set D_{HQC} is characterized by three maxima around 1480, 1640, and 1760 CE, which are subdued or absent, in the other data sets. The 1760 CE maximum can be more precisely described as a brief plateau lasting until ~1800 CE, while the trend of D_{MQC} and D_{LQC} for this period roughly coincides with that of BIGMUDI4k.1. A notable increase of $|g_1^0|$ around 1650 CE can also be observed for D_{MQC} and much less for D_{LQC}.

However, direct g_1^0 estimates are affected by large uncertainties (see shaded bands in Figure 2). Additional uncertainties very likely arise from the combination of poor spatial coverage and nondipole components, especially in the case of D_{HQC}. In such cases, the benefits of higher data quality might be nullified by the uncertainties associated with excessive data sparsity. This consideration underlines that a global model with higher order field components derived from the better geographical distribution of historical records is required for a correct assessment of the recent evolution of the dipole component. Therefore, a spherical harmonic modeling approach is applied to direct and indirect records as explained in the next section.

3. Geomagnetic Field Modeling

3.1. Global Field Models

The historical geomagnetic field evolution is reconstructed by applying a Bayesian inversion approach (Arneitz et al., 2019; Leonhardt & Fabian, 2007). The model uses a spherical harmonic expansion and cubic B-splines to describe field variations in the spatial and temporal domains, respectively. The geomagnetic field vector $\boldsymbol{B}_i(t_i,\theta_i,\phi_i)$ for a given time t_i, longitude ϕ_i, and colatitude θ_i is defined as the gradient of the scalar potential $\Phi(\boldsymbol{G}(t_i),\theta_i,\phi_i)$, where $\boldsymbol{G}(t_i)$ is the vector of Gauss coefficients g_l^m and h_l^m up to the maximum degree L as a function of time. The inversion problem of finding a field model that fits the observations is solved by minimizing $\frac{1}{2}\chi^2 + Q$ where χ^2 is the sum of squared model residuals and Q a regularization term. Model residuals

$$\chi^2 = \sum_{i=1}^{n}\left(\frac{\boldsymbol{E}_i \cdot \Re(\mathfrak{B}_i)\cdot[\hat{\boldsymbol{B}}_i + \nabla\Phi(\mathbf{G}_{\boldsymbol{\Gamma}}(t_i),R_{\mathrm{E}},\theta_i,\phi_i)]}{\delta\hat{\boldsymbol{B}}_i}\right)^2 \tag{1}$$

are first calculated in the local B_X, B_Y, and B_Z coordinate system at the Earth's surface (at radius R_{E}). This allows to handle different types of data by complementing missing components in incomplete records $\hat{\boldsymbol{B}}_i$ with the geomagnetic components given by an a priori model $\mathfrak{B}$ that is iteratively updated (see below). These residuals are then transformed into FDI coordinates through a rotation matrix $\Re(\mathfrak{B}_i)$ and multiplied by the Boolean vector $\boldsymbol{E}_i$, whose components are 0 or 1 depending on the existence of F, D, and I in the original measurement (Arneitz et al., 2019). Individual residuals are normalized by prior data uncertainties $\delta\hat{\boldsymbol{B}}_i$, which include measurement errors, truncation errors of the spherical harmonic expansion, as well as correlated location errors for historical ship measurements as defined by Arneitz et al. (2019). The regularization term

$$Q = \frac{\lambda}{P_0 T}\int_0^T\sum_{l=1}^{L} S_l(\partial_t\mathbf{G}_{\boldsymbol{\Gamma}}(t))\mathrm{d}t \tag{2}$$

is defined as the total variational energy at the CMB derived from the time derivative of Mauersberger-Lowes spectrum (Lowes, 1974)

$$S_l' = S_l(\partial_t\boldsymbol{G}) = (l+1)\sum_{m=0}^{l}(\partial_t g_l^m)^2 + (\partial_t h_l^m)^2. \tag{3}$$

The variational energy is normalized by an a priori estimate $P_0 = 1.6\ \mu\mathrm{T}^2/\mathrm{year}^2$ of the variational power, which has been derived from a Giant Gaussian Processes model by Constable and Parker (1988) and an autocorrelation time $\tau = 200$ years (Arneitz, Egli, & Leonhardt, 2017), multiplied by the duration T of the modeling period. The regularization parameter λ controls the adjustable trade-off between data fitting and energy fluctuation minimization.

The field guess $\mathfrak{B}$ used for the coordinate system rotation in Equation 1 is updated iteratively, starting from an initial guess. Stable convergence for any initial guess of $\mathfrak{B}$ was obtained through the stepwise inclusion of increasingly incomplete records, starting with full vector data in the first iteration step. This iterative approach is not strictly required, since the same modeling results are achieved by using all records in only two inversion steps. In this study, two inversion steps are used, since it reduces the computational efforts (see Figure S2 in Supporting Information S1, for the convergence behavior).

Because the spatiotemporal data density is higher during the historical epoch than for previous periods, the original spatial and temporal resolution of BIGMUDI4k.1 has been increased to a maximum spherical harmonic degree of $L = 10$ and a spline knot spacing of 10 years. Boundary conditions at 1380 CE and 1920 CE correspond to the global field configurations predicted by BIGMUDI4k.1 (using the mean coefficients from the bootstrap ensemble) and by the IGRF model of 1920 CE (Alken et al., 2021), respectively. The same regularization parameter $\lambda = 6.6$ as for the third and fourth inversion steps of BIGMUDI4k.1 is used here.

Null models, obtained using nominal direct and indirect data values without bootstrapping, have been computed with the above algorithm. Selection criteria described in the previous section have been applied to

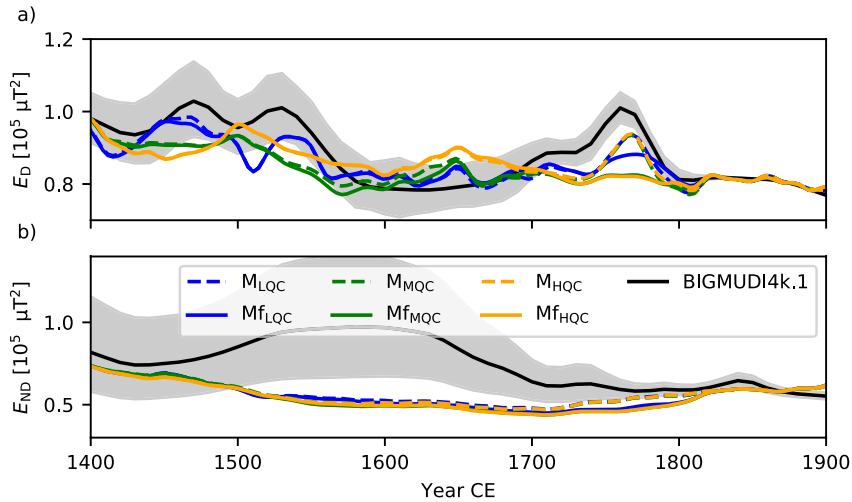

Figure 3. Temporal evolution of the dipolar (a) and nondipolar (b) energy at the core-mantle boundary for null models $M(f)_{LQC}$, $M(f)_{MQC}$, and $M(f)_{HQC}$, associated to the data sets D_{LQC}, D_{MQC}, and D_{HQC}, respectively. The results of BIGMUDI4k.1 are shown for comparison. Dashed lines refer to modeling results obtained from complete data sets, while solid lines represent models with outlier rejection.

archeointensity records yielding three different models M_{LQC}, M_{MQC}, and M_{HQC}. Outliers with residuals exceeding three standard deviations of the empirical residual distribution have been rejected. Outlier rejection has been performed separately for the direct and indirect records because of the strongly contrasting uncertainties associated with these two categories (see Figures S3–S8 in Supporting Information S1). This results in the final outlier-corrected null models Mf_{LQC}, Mf_{MQC}, and Mf_{HQC}. The effect of outlier rejection, which includes nearly the same records for each individual model (see Figures S9 and S10 in Supporting Information S1), is most prominent for CMB dipole energies around 1770 CE (Figure 3a), where a pronounced peak produced by all three data sets appears to be entirely controlled by the rejected records. The outlier rejection does not produce significant differences during earlier epochs, when complete and outlier-free data sets yield variations similar to those obtained directly from g_1^0 estimates (Figure 2), for example, around 1500 and 1650 CE for D_{HQC}. The nondipole energy (Figure 3b) is characterized by a much smoother time evolution, due to the stronger effect of regularization on higher spherical harmonic terms. For this reason, the nondipole energy is also insensitive to data selection and outlier rejection.

The role of regularization is also demonstrated by the different sensitivity of the dipole (E_D) and nondipole (E_{ND}) energy toward boundary conditions. For instance, replacing the 1380 CE field model from BIGMUDI4k.1 with an axial dipole affects E_D only during the first ~100 years (Figure 4a), while the effects on E_{ND} persist until ~1800 CE (Figure 4b). This means that E_{ND} is strongly controlled by the boundary conditions over the early centuries of the modeling period, which are characterized by a relatively low data density.

Differences between null models are dominated by field intensity F, which is in turn mainly related to the dipole term. An exemplary comparison of models Mf_{LQC} and Mf_{HQC} illustrates these differences in the temporal range (Figure S11a in Supporting Information S1). This is not surprising since data sets differ only in the archeointensity selection criteria. Minor differences can also be observed for inclination I, while a good agreement is observed for declination D, which is constrained by numerous historical records. In the spatial range, highest differences between Mf_{LQC} and Mf_{HQC} are found in Central Asia (Figure S11b in Supporting Information S1), where a lack of high-quality (D_{HQC}) intensity data can be observed (Figure 1a).

Null models support a preliminary evaluation of geomagnetic variations and can be used to test the effects of data selection, outlier removal, and regularization; however, a model ensemble (e.g., Licht et al., 2013) is required for the quantitative determinations of modeling uncertainties as discussed in Section 3.2. With this approach, data and age uncertainties as well as quality categories can be more specifically handled.

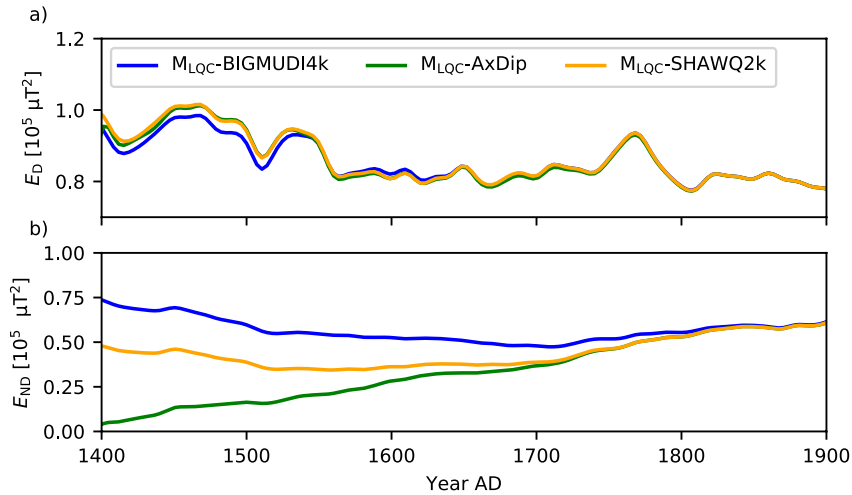

Figure 4. Temporal evolution of the dipolar (a) and nondipolar (b) energy at the core-mantle boundary for null model M_{LQC} with different lower boundary conditions in 1380 CE: M_{LQC}-BIGMUDI4k using BIGMUDI4k.1 predictions (Arneitz et al., 2019), M_{LQC}-AxDip using an axial dipole ($g_1^0 = -30\,\mu$T), and M_{LQC}-SHAWQ2k using SHAWQ2k predictions (Campuzano et al., 2019).

3.2. A New Bootstrapping Approach

The tests discussed in the previous section demonstrate the central role played by data selection and outlier rejection. Insufficient or excessive data selection is detrimental to model stability for opposite reasons: poor data quality and outliers introduce artifacts, such as the dipole energy peak at ~1770 CE (Figure 3a), while the elimination of too many records leads to poor temporal and spatial coverage, especially in the Eastern Hemisphere. Therefore, a trade-off must be found between the opposed needs of data quality and coverage.

A new bootstrapping approach dealing with this problem is developed. It is based on a jackknife procedure that always keeps high-quality records from data set D_{HQC}, while the remaining archeointensity records are randomly rejected or accepted. This empirical approach replaces a more objective approach based on a proper weighting of archeointensity records according to the existence of cooling rate and anisotropy corrections or the need of such corrections. This choice is motivated by the fact that uncertainties associated with the lack of cooling rate and anisotropy corrections are difficult to assess with meta information currently provided by archeomagnetic databases. About 620 archeointensities (~60% of all indirect intensity records) are included on average in each bootstrap run. All outliers detected in the null models M_{LQC}, M_{MQC}, and M_{HQC} are excluded from the bootstrapping procedure. Variations of input data, redundancy, and regularization parameter (λ is kept fixed for the first inversion step) closely follow the approach applied by Arneitz et al. (2019). However, missing information on age uncertainties is now considered by assigning a default error of ±40 years, which corresponds to the median uncertainty of all archeomagnetic records. The field model used for the 1380 CE boundary condition is randomly selected from the BIGMUDI4k.1 bootstrapping ensemble in each simulation.

An ensemble of 500 bootstrap simulations has been calculated with the method described above (available at https://cobs.zamg.ac.at/data/index.php/en/models-and-databases/geomagnetic-model). Average quantities (e.g., field elements and energies) along with their uncertainties, identified with ensemble standard deviations, represent the effective model output of BIGMUDIh.1. Not surprisingly, BIGMUDIh.1 yields a much smoother temporal evolution of the dipole energy at the CMB compared to the null models Mf_{LQC}, Mf_{MQC}, and Mf_{HQC} (Figure 3a vs. Figure 5b). Furthermore, BIGMUDIh.1 does not strongly correlate with short-term variations of any of the null models, which means that it is not dominated by a specific data subset (Figure 5a). Differences between the ensemble solution and the null models Mf_{LQC}, Mf_{MQC}, and Mf_{HQC} are mostly smaller than the 2σ limit of bootstrapping uncertainties—the only exception being represented by Mf_{HQC} between 1620 and 1660 CE.

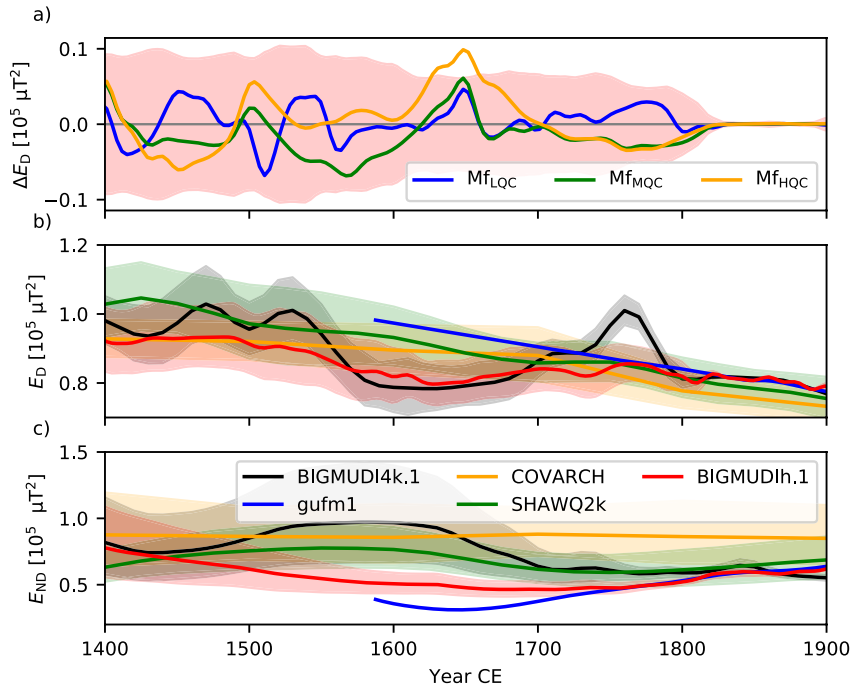

Figure 5. (a): Differences of dipole energies between individual models (Mf$_{LQC}$, Mf$_{MQC}$, and Mf$_{HQC}$) and bootstrapping model BIGMUDIh.1 along with 2σ bootstrapping uncertainties (shaded area). Temporal evolution of the dipolar (b) and nondipolar (c) energy at the core-mantle boundary for bootstrapping results BIGMUDIh.1 compared to other geomagnetic models.

In the following, we compare BIGMUDIh.1 with four models that cover the historical time interval: SHAWQ2k (Campuzano et al., 2019), COVARCH (Hellio & Gillet, 2018), gufm1 (Jackson et al., 2000), and BIGMUDI4k.1 (Arneitz et al., 2019). The latter two models have been selected since they are (partly) based on historical records. The choice of SHAWQ2k and COVARCH is justified by the fact that these purely archeomagnetic models are based on similar, recently published data sets and, like BIGMUDIh.1, are free from artifacts introduced by sedimentary records. Furthermore, they have not been constructed by penalizing deviations from the gufm1 model for the historical era. The weighting scheme for high-quality archeomagnetic data applied for SHAWQ2k additionally yields a valuable comparison with our approach.

A continuous decrease of dipole energy at the CMB during the 16th century can be observed in BIGMUDIh.1 reconstructions (Figure 5b). This decrease starts earlier than in BIGMUDI4k.1 results and is not so steep. From 1600 CE onward, no major dipole variations are found. The peak around 1760 CE predicted by BIGMUDI4k.1 is almost completely suppressed. The field models gufm1, due to the fixed linear extrapolation of g_1^0, and SHAWQ2k yield a quasilinear decrease of dipole energy for the historical epoch. The dipole energy decrease of COVARCH is small until 1700 CE, when a steeper decline occurs and continues for the following 200 years. As far as nondipole contributions are concerned (Figure 5c), field reconstructions from SHAWQ2k, COVARCH, and BIGMUDI4k.1 yield higher energies during the 16th, 17th, and 18th centuries compared to BIGMUDIh.1 and gufm1. For the latter two models, a strong agreement is found from the middle of the 18th century CE onward.

Differences in the evolution of nondipole energies are also reflected by the time-averaged power spectra (Figure S12 in Supporting Information S1). Similar energy terms are predicted by all field reconstructions for degrees $l = 1 - 5$ (Figure S12a in Supporting Information S1). At higher degrees, however, BIGMUDIh.1 and gufm1 energies exceed those predicted by COVARCH (starting from $l = 6$) and by SHAWQ2k (starting from $l = 9$). These differences are most likely caused by the additional geomagnetic information provided by historical records, which is missing in the case of purely archeomagnetic models. The power spectrum of secular variation (SV) is characterized by significantly higher dipole energies for BIGMUDIh.1 and BIGMUDI4k.1 reconstructions (Figure S12b in Supporting Information S1). The higher dipole energy is related

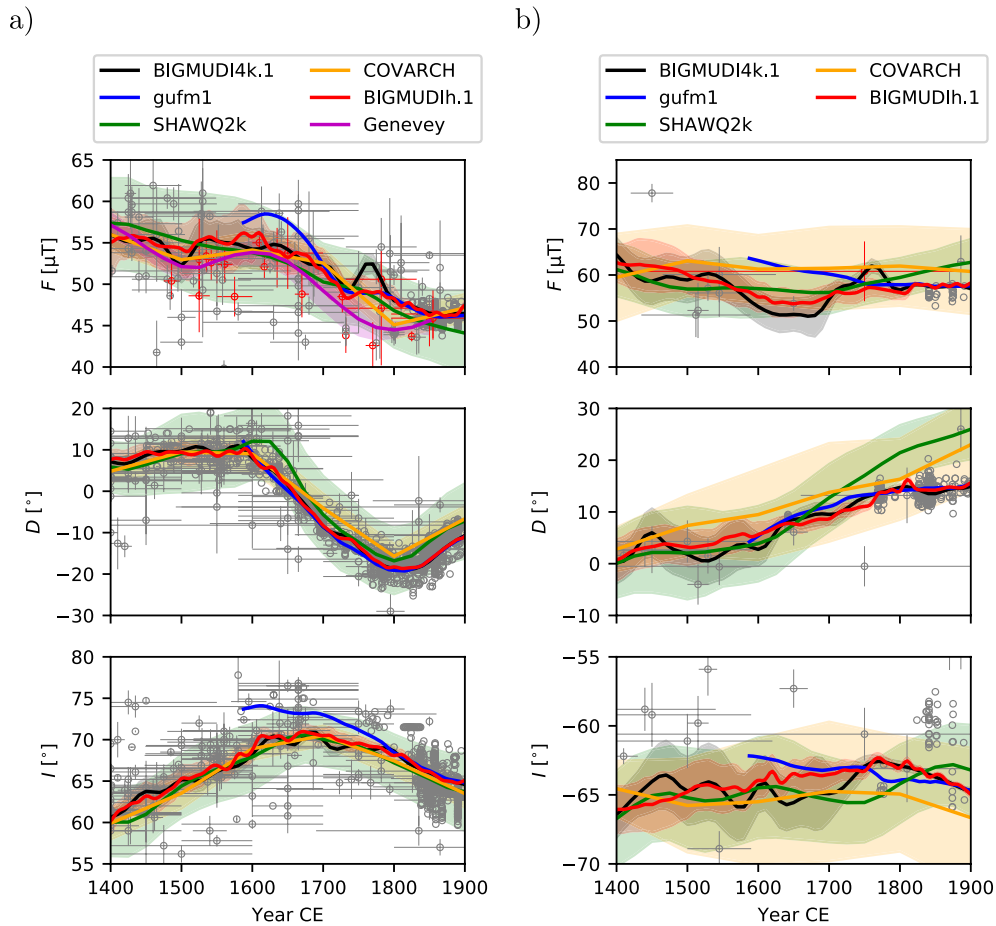

Figure 6. Times series of F (top), D (middle), and I (bottom) for different modeling approaches in Central Europe (a) and New Zealand (b). Modeling input records within a radius of 750 km are given by gray circles, while D_{HQC} high-quality archeointensities are depicted in red. Note that input data values (for I and F) are not converted to the reference site. In (a), the regional intensity curve for Paris (Genevey et al., 2016) is depicted.

to larger short-term fluctuations with a period of ~20–30 years observed in the time series of geomagnetic components (Figure 6). They can be linked to the regularization approach through the systematically smaller damping of dipole fluctuations with respect to nondipole fluctuations for a wide range of regularization parameters. This requires a reassessment of the regularization approach in future models. Nevertheless, the reconstructed field and its long-term variations remain unaffected. In the case of nondipole SV terms, a nearly flat spectrum can be observed for BIGMUDIh.1, up to $l = 7$, and gufm1, while SHAWQ2k and COVARCH show a more pronounced decrease starting from $l = 7$ and $l = 6$, respectively.

The effects of different modeling approaches can be further inspected by comparing predicted geomagnetic field components at the Earth's surface. For this purpose, two regions in Central Europe (Nürnberg, 49.4°N, 11.1°E) and New Zealand (40°S, 175°E) have been selected, representing the cases of high- and low-data density within a radius of 750 km, respectively (Figure 6). In general, modeled geomagnetic directions agree well within Central Europe (Figure 6a). The only obvious deviation is given by the steeper gufm1 inclinations prior to 1800 CE. On the other hand, the detailed evolution of F differs from the regional SV curve in Paris (Genevey et al., 2016), which is characterized by a more pronounced minimum at the end of the 18th century. A similar temporal intensity evolution has been recently proposed using Triaxe measurements from Uzbekistan (Troyano et al., 2021). In Central Europe, however, this hypothetical intensity minimum cannot be confirmed due to the relatively large dispersion of archeointensity records around 1800 CE.

Directional model predictions for New Zealand agree quite well within their uncertainties, despite the sparsity of reference records (Figure 6b). A moderate influence of historical D data is visible during the

late 18th and 19th centuries, when models that incorporate this type of data (gufm1, BIGMUDI4k.1, and BIGMUDIh.1) are compared with purely archeomagnetic models (SHAWQ2k and COVARCH). New archeointensity records from New Zealand, which are included in recent database updates, support the existence of a sharp intensity peak in the early fifteenth century (Turner et al., 2020). Generally, the ability of global field models to resolve such strong and rapid geomagnetic variations is rather limited (e.g., Davies & Constable, 2017), which is reflected by the relatively weak intensity decrease around 1500 CE predicted by BIGMUDIh.1. A further issue of interest for future modeling and data selection approaches is related to the recently published New Zealand data set; differences in natural and laboratory cooling rates have been estimated as negligible, causing only slight overestimates within data uncertainties (Turner et al., 2020). Therefore, these records could have actually been considered as high-quality records, which were not the case for BIGMUDIh.1 due to the missing cooling rate correction. This circumstance underlines the need for more differentiated meta information in the available databases in order to avoid reevaluation of (numerous) individual archeomagnetic studies.

Finally, a global-scale comparison between the field models incorporating historical records is performed (Figures S13–S14 in Supporting Information S1). On average, a strong agreement between BIGMUDIh.1 and gufm1 (Figure S13 in Supporting Information S1) for declination predictions between 1590 and 1900 CE is found, which is expected because of the dominant role of historical ship log data (Jonkers et al., 2003). In contrast, gufm1 yields significantly higher F predictions within the 17th and 18th centuries, especially in the southern South American and New Zealand regions (Figure 6b), which is also reflected by the different dipole energy evolutions (Figure 5b). Inclination differences prior to 1800 CE originate from higher spherical harmonic degrees, with gufm1 generally predicting steeper inclinations in the Northern Hemisphere and shallower ones in the Southern Hemisphere, except around the polar regions (Figure S13d in Supporting Information S1).

A similar picture is revealed from the comparison of BIGMUDIh.1 and BIGMUDI4k.1 for the time interval between 1400 and 1900 CE (Figure S14 in Supporting Information S1). Globally, the averaged differences in F predictions are mainly driven by differing dipole reconstructions, for instance, around 1500 and 1770 CE (Figure S14a in Supporting Information S1). Highest intensity differences are found in the Western hemisphere around North and South America, where BIGMUDIh.1 predicts systematically lower field strengths with respect to BIGMUDI4k.1 (Figure S14b in Supporting Information S1). A more complex behavior, with stronger contributions from the nondipole terms, is observed for the differences between geomagnetic directions (Figures S14c and S14d in Supporting Information S1). These observations underline the impact of new and revised input data used for BIGMUDIh.1 construction.

4. Discussion

The evolution of the historical axial dipole coefficient $|g_1^0|$ predicted by different models is illustrated in Figure 7. BIGMUDIh.1 predicts a ~0.019 μT/yr decrease between 1500 and 1600 CE, which agrees well with the 0.018 μT/yr decline from 1900 CE onward given by IGRF models (e.g., Alken et al., 2021). BIGMUDIh.1 yields a period of stable $|g_1^0|$ values around 32.5 ± 0.5 μT from 1600 to 1900 CE. This is in agreement with estimates by Gubbins et al. (2006) and the final conclusions of Finlay (2008), while the linear 0.015 μT/yr decrease between 1600 and 1840 CE assumed by Jackson et al. (2000) is also observed in the SHAWQ2k model (0.014 μT/yr). A minimum of the axial dipole intensity determined from the regional archeointensity data sets within the second half of the 18th century (e.g., Troyano et al., 2021) is not confirmed by the other (global) models.

Arneitz et al. (2019) investigated the connection of the steep $|g_1^0|$ decline (~0.07 μT/yr) during the 16th century and the subsequent dipole minimum predicted by BIGMUDI4k.1 around 1600 CE with the emergence of the numerous historical D-records. They could not find convincing evidence of modeling artifacts within this time period, but underlined the need for new intensity records in order to better constrain the dipole evolution. Fortunately, new archeointensity records covering critical periods and regions are now available (e.g., Kapper et al., 2020; Turner et al., 2020). These updates enable a better characterization of the global field behavior. The new data constellation leads to a moderate decrease of $|g_1^0|$ during the 16th century with a 30–40- year earlier onset in BIGMUDIh.1.

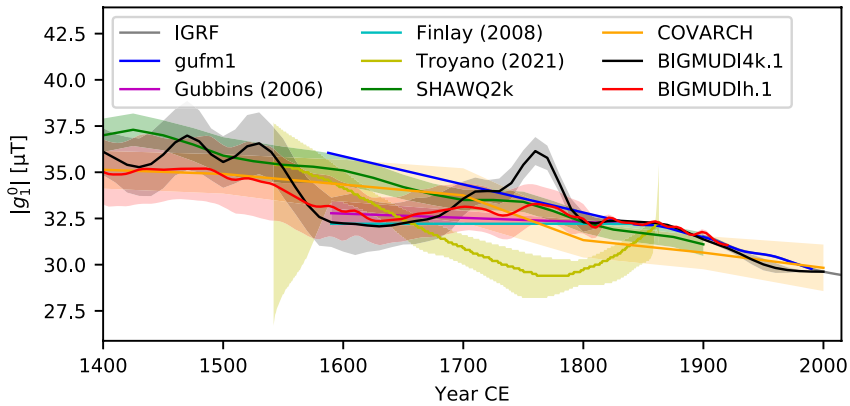

Figure 7. Temporal evolution of $|g_1^0|$ predicted by different models.

The second highly remarkable axial dipole feature of BIGMUDI4k.1 was the strong maximum around 1760 CE, which is almost completely absent in the new BIGMUDIh.1 results. The reason for this difference can be found in a combination of database updates and, more importantly, outlier rejection as tested on the null models $M(f)_{MQC}$ and $M(f)_{HQC}$ (Figure 3). Interestingly, rejection comprises, besides several directional data, a single archeointensity record featuring an unrealistically large field intensity (90 μT) in the USA (Sternberg, 1989). This anomalous intensity value might be caused by the production of the investigated archeological artifacts inside iron kiln furnitures (Suttie et al., 2011). This record has not been rejected during BIGMUDI4k.1 constructions, because generally the larger model residuals caused by the inclusion of previous epochs with sparse data (along with potentially higher uncertainties) would not spot such high archeointensity values as outliers. Alternatively, new archeointensity records from the USA (Jones et al., 2020) might have led to a stronger deviation of the considered record from BIGMUDIh.1 intensity predictions and consequently to its rejection. Moreover, it is noteworthy that several historical inclination measurements on ship voyages have been rejected in the second half of the 18th century (Figure S9 in Supporting Information S1). Nevertheless, the 1760 CE axial dipole peak of individual models M_{LQC}, M_{MQC}, and M_{HQC}, which include outliers, is still less pronounced than in BIGMUDI4k.1 (Figure 3a). While the true origin of the major differences between BIGMUDI reconstructions remains somehow uncertain, the potential impact of a few records on model results during critical periods needs to be considered. This underlines the need for the future scrutiny of outlier evaluation and rejection methods.

The geomagnetic field modulates, together with the heliospheric magnetic field (HMF), the radionuclide production in the Earth's atmosphere by deflecting cosmic particles due to the Lorentz force (e.g., Herbst et al., 2017). Pavón-Carrasco et al. (2018) related multicentennial fluctuations of radionuclide production to the geomagnetic field variations, mainly driven by the axial dipole strength with contributions of up to 7% from the nondipole terms. However, for shorter timescales, like the time interval studied here, a major influence of the HMF on cosmogenic radionuclides exists (Brehm et al., 2021) and no correlation between ^{14}C production and axial dipole intensity is found (Figure S15 in Supporting Information S1).

The temporal evolution of field intensity F at the Earth's surface and radial component B_r at the CMB is depicted in Figure 8. The evolution of the SAA, an area of low-field intensity, over Southern Africa and its subsequent growth and westward motion toward South America can be observed. The SAA is produced by RFPs at the CMB, currently located beneath Patagonia, the South Atlantic, and South Africa (see, e.g., Pavón-Carrasco & De Santis, 2016; Terra-Nova et al., 2017). The origin of these RFPs was recently traced back in time by SHAWQ2k and BIGMUDI4k.1: Campuzano et al. (2019) found an area of reverse flux penetrating from South of India toward Southern Africa around 1000 CE. A similar evolution is captured by BIGMUDI4k.1 already around 100 CE, followed by periods of changing RFP amplitude and extent around Southern Africa and America (see Video 1 in Supporting Information by Arneitz et al., 2019). Therefore, BIGMUDIh.1 reconstructions do not capture the emergence of the SAA, but track the temporal evolution of distinct flux patches more closely over the historical period. In 1400 and 1500 CE (Figures 8a and 8b), a prominent RFP is located around Southern Africa, which is split into two parts around 1600 CE (Figure 8c).

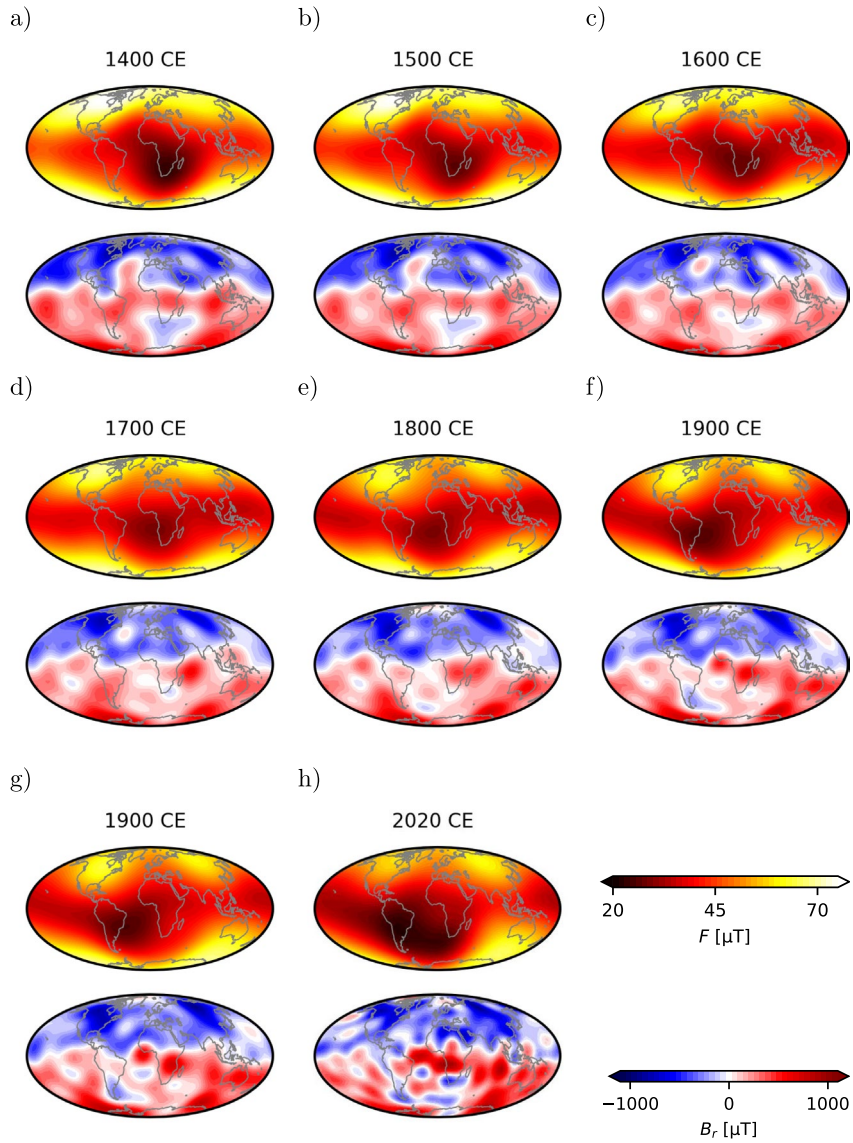

Figure 8. Field intensity F at the Earth's surface (top) and radial field component B_r at the core-mantle boundary (bottom) predicted by BIGMUDIh.1 (a–f) and IGRF models (g–h) for different periods.

Around 1700 CE (Figure 8d), a third RFP (besides those detected in 1600 CE in Southern Africa and at lower latitudes in the Atlantic) arises at higher latitudes north of Antarctica and gains in strength and area until 1800 CE (Figure 8e), when the other two RFPs are clearly weakened. Throughout the 19th century, the increase and westward movement of the RFP from higher latitudes toward South America can be observed (Figure 8f). IGRF models (e.g., Alken et al., 2021) describe a reinvigoration for the RFP east of Southern Africa as well as an increase in area and strength for the Patagonian RFP over the last century, leading to the current complex picture (Figures 8g and 8h). Subtle, small-scale differences exist between the extension, location, and displacement of RFPs predicted by BIGMUDIh.1 and BIGMUDI4k.1. They might arise, in part, from the different spatiotemporal resolution of the two models. On the other hand, while SHAWQ2k reconstructions (up to $L = 6$) indicate that the SAA evolution was driven by a single RFP (Campuzano et al., 2019), the incorporation of historical data for BIGMUDI models suggests a more complex field evolution at the CMB from ~1600 CE onward.

Another area of reversed magnetic flux at the CMB is currently located beneath the northern polar region (Figure 8h). Its emergence from equatorial regions can be traced back to 1000–1400 CE from SHAWQ2k

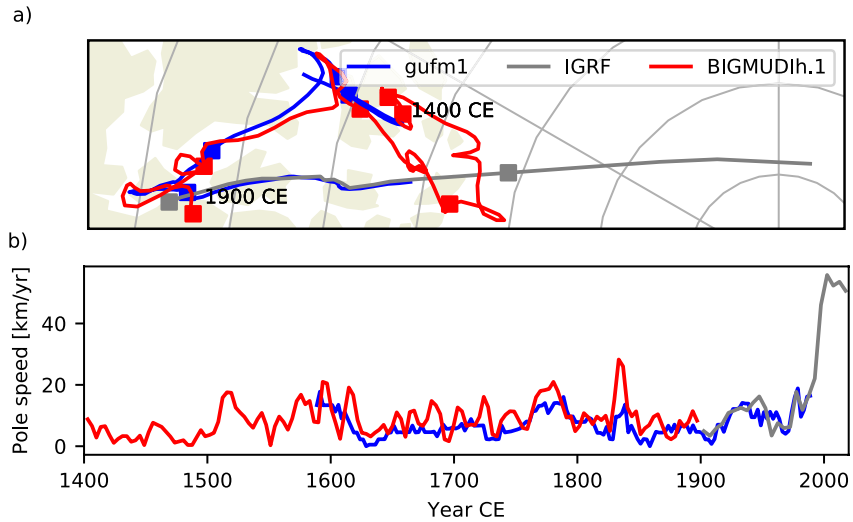

Figure 9. (a): Magnetic north dip pole wandering paths given by different models. The beginning of different centuries is depicted by squares. (b): Reconstructed pole speeds.

and BIGMUDI4k.1 reconstructions, respectively. According to BIGMUDIh.1, the RFP reached its present high-latitude position within the 18th century, potentially affecting the migration of the north magnetic dip pole (Olsen & Mandea, 2007). Throughout the historical epoch, the north magnetic pole drift (Figure 9) is limited to moderate speeds (in general <20km/yr) within the Western hemisphere (Canadian Arctic), while in recent years, an acceleration to >50km/yr toward Siberia was observed (e.g., Livermore et al., 2020). The Canadian and Siberian flux lobes are affecting the position of the magnetic North Pole during the last decades: weakening of the Canadian flux patch produces the observed pole acceleration toward East (Livermore et al., 2020). BIGMUDIh.1 predicts two periods of relatively high pole speed (>20km/yr) around 1775 and 1835 CE, which are also observed, in an attenuated manner, using gufm1 reconstructions. These periods can be connected to the evolution of RFPs in the Northern Hemisphere. An increase of the RFP beneath Greenland is observed in the second half of the 18th century (Figure S16a in Supporting Information S1), while a new RFP occurs in the northern Pacific area during the first half of the 19th century (Figure S16b in Supporting Information S1). A direct influence of RFPs on current high pole speeds has been ruled out (Livermore et al., 2020). However, this study suggests that moderate acceleration of pole movements within the historical epoch could have been influenced by emergence and evolution of RPFs in or adjacent to the polar region.

5. Conclusions

In this study, a new spherical harmonic geomagnetic field model BIGMUDIh.1 was developed for the time interval covered by historical records (i.e., between 1400 CE and 1900 CE). The inversion approach combines direct and indirect field records with widely contrasting distributions and uncertainties using optimized weighting procedures (Arneitz et al., 2019; Leonhardt & Fabian, 2007). The quality of different archeointensity records is taken into account by the bootstrapping process, which in each run randomly rejects a subset of the lower quality data, but always retains the high-quality data.

The incorporation of archeointensities allows for a direct estimation of the axial dipole evolution prior to 1840 CE in contrast to the established historical model gufm1 (Jackson et al., 2000). Contrary to the linear extrapolation of g_1^0 assumed for gufm1 construction, BIGMUDIh.1 predicts a steady dipole intensity decrease between 1500 and 1600 CE, followed by a period of approximately constant axial dipole behavior until 1900 CE. The variations in declination predicted by gufm1 and BIGMUDIh.1 agree very well, because they are strongly confined by instrumental data with a high spatial and temporal coverage. While the limited period of time covered by the model does not permit to reconstruct the emergence of the SAA—which is observed in archeomagnetic models at least for the last millennium (Arneitz et al., 2019; Campuzano et al., 2019)—,a complex evolution of three RFPs in Southern America, Atlantic, and Africa is captured

by BIGMUDIh.1 over the last centuries. RFPs in the Northern Hemisphere could also be the source of the moderately accelerated magnetic pole movement (of >20 km/yr) within the historical time intervals.

The thorough analysis of data selection criteria and outlier rejection (Figures 2 and 3) underlines the crucial impact of the data handling procedure. Astonishingly, in spite of decades of archeomagnetic data collection, not even the evolution of the most prominent dipole term over the most recent pre-instrumental centuries is clearly defined by the data, and the estimates are still strongly influenced by local data groups. This emphasizes the need for the new high-quality archeomagnetic records for better constraining the historical field evolution in more detail, especially in the Southern and Eastern Hemispheres. Geomagnetic data compilations would considerably benefit from additional measurement and processing information, which would simplify an a priori detection of outlier and allow for an in-depth assessment of data reliability. In this context, statistical evaluations of experimental protocols at the site level (e.g., Arneitz, Egli, & Leonhardt, 2017; Pavón-Carrasco et al., 2016; Suttie et al., 2011) as well as at raw data level (e.g., Paterson et al., 2014, 2017), for example, provided by MagIC database (Jarboe et al., 2012), support the development of new guidelines for improved data selection criteria and weighting procedures.

Data Availability Statement

The data used in this study are available at https://cobs.zamg.ac.at/data/index.php/en/models-and-databases/histmag. Modeling results can be found at https://cobs.zamg.ac.at/data/index.php/en/models-and-databases/geomagnetic-model.

Acknowledgments
P. Arneitz acknowledges funding from the BMBWF project E21-COBSSTRUKTUR21 (1410K214018E). We are grateful for the constructive comments of two anonymous reviewers that helped to significantly improve the manuscript.

References

Alken, P., Thébault, E., Beggan, C. D., Amit, H., Aubert, J., Baerenzung, J., et al. (2021). International geomagnetic reference field: The thirteenth generation. *Earth, Planets and Space*, *73*(1), 1–25. https://doi.org/10.1186/s40623-020-01281-4

Arneitz, P., Egli, R., & Leonhardt, R. (2017). Unbiased analysis of geomagnetic data sets and comparison of historical data with paleomagnetic and archeomagnetic records. *Reviews of Geophysics*, *55*(1), 5–39. https://doi.org/10.1002/2016RG000527

Arneitz, P., Egli, R., Leonhardt, R., & Fabian, K. (2019). A Bayesian iterative geomagnetic model with universal data input: Self-consistent spherical harmonic evolution for the geomagnetic field over the last 4000 years. *Physics of the Earth and Planetary Interiors*, *290*, 57–75. https://doi.org/10.1016/j.pepi.2019.03.008

Arneitz, P., Leonhardt, R., Schnepp, E., Heilig, B., Mayrhofer, F., Kovacs, P., et al. (2017). The HISTMAG database: Combining historical, archaeomagnetic and volcanic data. *Geophysical Journal International*, *210*(3), 1347–1359. https://doi.org/10.1093/gji/ggx245

Aubert, J., Aurnou, J., & Wicht, J. (2008). The magnetic structure of convection-driven numerical dynamos. *Geophysical Journal International*, *172*(3), 945–956. https://doi.org/10.1111/j.1365-246x.2007.03693.x

Barraclough, D. R. (1974). Spherical harmonic analyses of the geomagnetic field for eight epochs between 1600 and 1910. *Geophysical Journal International*, *36*(3), 497–513. https://doi.org/10.1111/j.1365-246X.1974.tb00611.x

Biggin, A. J., Bono, R. K., Meduri, D. G., Sprain, C. J., Davies, C. J., Holme, R., & Doubrovine, P. V. (2020). Quantitative estimates of average geomagnetic axial dipole dominance in deep geological time. *Nature Communications*, *11*(1), 1–9. https://doi.org/10.1038/s41467-020-19794-7

Brehm, N., Bayliss, A., Christl, M., Synal, H.-A., Adolphi, F., Beer, J., et al. (2021). Eleven-year solar cycles over the last millennium revealed by radiocarbon in tree rings. *Nature Geoscience*, *14*(1), 10–15. https://doi.org/10.1038/s41561-020-00674-0

Brown, M., Donadini, F., Korte, M., Nilsson, A., Korhonen, K., Lodge, A., et al. (2015). GEOMAGIA50.v3: 1. general structure and modifications to the archeological and volcanic database. *Earth, Planets and Space*, *67*(1), 83. https://doi.org/10.1186/s40623-015-0232-0

Campuzano, S., Gómez-Paccard, M., Pavón-Carrasco, F., & Osete, M. (2019). Emergence and evolution of the South Atlantic Anomaly revealed by the new paleomagnetic reconstruction SHAWQ2k. *Earth and Planetary Science Letters*, *512*, 17–26. https://doi.org/10.1016/j.epsl.2019.01.050

Constable, C. G., & Parker, R. L. (1988). Statistics of the geomagnetic secular variation for the past 5 m.y. *Journal of Geophysical Research*, *93*(B10), 11569–11581. https://doi.org/10.1029/JB093iB10p11569

Dalrymple, A., Cavendish, H., & Abercrombie, B. (1778). XIX. Journal of a voyage to the East Indies: In the Ship Grenville, Captain Burnet Abercrombie. In *The year 1775 (No. 68)*. Philos. Trans. R. Soc. London.

Davies, C., & Constable, C. (2017). Geomagnetic spikes on the core-mantle boundary. *Nature Communications*, *8*, 15593. https://doi.org/10.1038/ncomms15593

de los Rios, H. (1621). Variaciones del aguja observadas por el licenciado Hernando de los Rios Coronel procurador de las islas Filipinas [Manuscript Mss/3190]. In D. Ramírez de Arellano (Ed.), *Reconocimiento de los estrechos de Magallanes y San Vicente, con algunas cosas curiosas de navegación*. Biblioteca Nacional de Espana. Retrieved from http://bdh-rd.bne.es/viewer.vm?id=0000087033&page=1

Ferk, A., Leonhardt, R., Hess, K.-U., Koch, S., Egli, R., Krása, D., & Dingwell, D. B. (2014). Influence of cooling rate on thermoremanence of magnetite grains: Identifying the role of different magnetic domain states. *Journal of Geophysical Research: Solid Earth*, *119*(3), 1599–1606. https://doi.org/10.1002/2013JB010845

Finlay, C. C. (2008). Historical variation of the geomagnetic axial dipole. *Physics of the Earth and Planetary Interiors*, *170*(1), 1–14. https://doi.org/10.1016/j.pepi.2008.06.029

Gallet, Y., & Le Goff, M. (2006). High-temperature archeointensity measurements from Mesopotamia. *Earth and Planetary Science Letters*, *241*(1), 159–173. https://doi.org/10.1016/j.epsl.2005.09.058

Gauss, C. F. (1833). Die Intensität der erdmagnetischen Kraft, zurückgeführt auf absolutes Maass. *Annalen der Physik*, *104*(6), 241–273. https://doi.org/10.1002/andp.18331040602

Genevey, A., Gallet, Y., Jesset, S., Thébault, E., Bouillon, J., Lefévre, A., & Le Goff, M. (2016). New archeointensity data from French Early Medieval pottery production (6th–10th century AD). Tracing 1500 years of geomagnetic field intensity variations in Western Europe. *Physics of the Earth and Planetary Interiors*, *257*, 205–219. https://doi.org/10.1016/j.pepi.2016.06.001

Genevey, A., Gallet, Y., Rosen, J., & Le Goff, M. (2009). Evidence for rapid geomagnetic field intensity variations in Western Europe over the past 800 years from new French archeointensity data. *Earth and Planetary Science Letters*, *284*(1), 132–143. https://doi.org/10.1016/j.epsl.2009.04.024

Gubbins, D., Jones, A. L., & Finlay, C. C. (2006). Fall in Earth's Magnetic Field Is Erratic. *Science*, *312*(5775), 900–902. https://doi.org/10.1126/science.1124855

Hansteen, C. (1819). *Untersuchungen über den Magnetismus der Erde* (Vol. 1). Gedruckt bey J. Lehmann und C. Gröndahl.

Heirtzler, J. R., Allen, J. H., & Wilkinson, D. C. (2002). Ever-present South Atlantic Anomaly damages spacecraft. *Eos, Transactions American Geophysical Union*, *83*(15), 165–169. https://doi.org/10.1029/2002eo000105

Hellio, G., & Gillet, N. (2018). Time-correlation-based regression of the geomagnetic field from archeological and sediment records. *Geophysical Journal International*, *214*(3), 1585–1607. https://doi.org/10.1093/gji/ggy214

Herbst, K., Muscheler, R., & Heber, B. (2017). The new local interstellar spectra and their influence on the production rates of the cosmogenic radionuclides ^{10}Be and ^{14}C. *Journal of Geophysical Research: Space Physics*, *122*(1), 23–34. https://doi.org/10.1002/2016ja023207

Hescoatt, J. (1684). *Log of Barnadistant. Manuscript, Sloane/854*. British Library.

Jackson, A., Jonkers, A. R. T., & Walker, M. R. (2000). Four centuries of geomagnetic secular variation from historical records. *Philosophical Transactions of the Royal Society A: Mathematical, Physical & Engineering Sciences*, *358*(1768), 957–990. https://doi.org/10.1098/rsta.2000.0569

Jarboe, N., Koppers, A., Tauxe, L., Minnett, R., & Constable, C. (2012). The online MagIC Database: Data archiving, compilation, and visualization for the geomagnetic, paleomagnetic and rock magnetic communities. In Agu fall meeting abstracts (Vol. 1, p. 1063).

Jones, S. A., Tauxe, L., Blinman, E., & Genevey, A. (2020). Archeointensity of the Four Corners Region of the American Southwest. *Geochemistry, Geophysics, Geosystems*, *21*(3), e2018GC007509. https://doi.org/10.1029/2018gc007509

Jonkers, A. R. T., Jackson, A., & Murray, A. (2003). Four centuries of geomagnetic data from historical records. *Reviews of Geophysics*, *41*(2). https://doi.org/10.1029/2002RG000115

Kapper, L., Serneels, V., Panovska, S., Ruíz, R. G., Hellio, G., de Groot, L., et al. (2020). Novel insights on the geomagnetic field in West Africa from a new intensity reference curve (0-2000 AD). *Scientific Reports*, *10*(1), 1–15. https://doi.org/10.1038/s41598-020-57611-9

Knepp, J. (1683). *Journals of J. Knepp on HMS Rose*. British Library.

Korte, M., Mandea, M., & Matzka, J. (2009). A historical declination curve for Munich from different data sources. *Physics of the Earth and Planetary Interiors*, *177*(3–4), 161–172. https://doi.org/10.1016/j.pepi.2009.08.005

Le Goff, M., & Gallet, Y. (2004). A new three-axis vibrating sample magnetometer for continuous high-temperature magnetization measurements: Applications to paleo- and archeo-intensity determinations. *Earth and Planetary Science Letters*, *229*(1–2), 31–43. https://doi.org/10.1016/j.epsl.2004.10.025

Leonhardt, R., & Fabian, K. (2007). Paleomagnetic reconstruction of the global geomagnetic field evolution during the Matuyama/Brunhes transition: Iterative Bayesian inversion and independent verification. *Earth and Planetary Science Letters*, *253*(1–2), 172–195. https://doi.org/10.1016/j.epsl.2006.10.025

Licht, A., Hulot, G., Gallet, Y., & Thébault, E. (2013). Ensembles of low degree archeomagnetic field models for the past three millennia. *Physics of the Earth and Planetary Interiors*, *224*, 38–67. https://doi.org/10.1016/j.pepi.2013.08.007

Livermore, P. W., Finlay, C. C., & Bayliff, M. (2020). Recent north magnetic pole acceleration towards Siberia caused by flux lobe elongation. *Nature Geoscience*, *13*(5), 387–391. https://doi.org/10.1038/s41561-020-0570-9

Lowes, F. J. (1974). Spatial power spectrum of the main geomagnetic field, and extrapolation to the core. *Geophysical Journal International*, *36*(3), 717–730. https://doi.org/10.1111/j.1365-246X.1974.tb00622.x

Malaspina, A., & Bustamante y Guerra, J. D. (1885). *Viaje político-científico alrededor del mundo por las corbetas descubierta y atrevida al mando de los capitanes de navío d. alejandro malaspina y don josé de bustamante y guerra desde 1789 á 1794, publicado con una introducción por don pedro de novo y colson teniente de navío académico correspondiente de la real de la historia*. Imprenta de la viuda é hijos de Abienzo.

Moore, T. E., & Horwitz, J. L. (2007). Stellar ablation of planetary atmospheres. *Reviews of Geophysics*, *45*(3). https://doi.org/10.1029/2005rg000194

Olsen, N., & Mandea, M. (2007). Will the magnetic North Pole move to Siberia? *Eos, Transactions American Geophysical Union*, *88*(29), 293–293. https://doi.org/10.1029/2007eo290001

Panovska, S., Constable, C. G., & Korte, M. (2018). Extending global continuous geomagnetic field reconstructions on timescales beyond human civilization. *Geochemistry, Geophysics, Geosystems*, *19*(12), 4757–4772. https://doi.org/10.1029/2018gc007966

Paterson, G. A., Muxworthy, A. R., Yamamoto, Y., & Pan, Y. (2017). Bulk magnetic domain stability controls paleointensity fidelity. *Proceedings of the National Academy of Sciences*, *114*(50), 13120–13125. https://doi.org/10.1073/pnas.1714047114

Paterson, G. A., Tauxe, L., Biggin, A. J., Shaar, R., & Jonestrask, L. C. (2014). On improving the selection of Thellier-type paleointensity data. *Geochemistry, Geophysics, Geosystems*, *15*(4), 1180–1192. https://doi.org/10.1002/2013GC005135

Pavón-Carrasco, F., Gomez-Paccard, M., Campuzano, S. A., González-Rouco, J., & Osete, M. L. (2018). Multi-centennial fluctuations of radionuclide production rates are modulated by the Earth's magnetic field. *Scientific Reports*, *8*(1), 9820. https://doi.org/10.1038/s41598-018-28115-4

Pavón-Carrasco, F. J., & De Santis, A. (2016). The South Atlantic Anomaly: The Key for a Possible Geomagnetic Reversal. *Frontiers of Earth Science*, *4*, 40. https://doi.org/10.3389/feart.2016.00040

Pavón-Carrasco, F. J., Gómez-Paccard, M., Hervé, G., Osete, M. L., & Chauvin, A. (2014). Intensity of the geomagnetic field in Europe for the last 3 ka: Influence of data quality on geomagnetic field modeling. *Geochemistry, Geophysics, Geosystems*, *15*(6), 2515–2530. https://doi.org/10.1002/2014GC005311

Pavón-Carrasco, F. J., Tema, E., Osete, M. L., & Lanza, R. (2016). Statistical analysis of palaeomagnetic data from the last four centuries: Evidence of systematic inclination shallowing in lava flow records. *Pure and Applied Geophysics*, *173*, 839–848. https://doi.org/10.1007/s00024-014-0946-0

Poletti, W., Biggin, A. J., Trindade, R. I., Hartmann, G. A., & Terra-Nova, F. (2018). Continuous millennial decrease of the Earth's magnetic axial dipole. *Physics of the Earth and Planetary Interiors*, *274*, 72–86. https://doi.org/10.1016/j.pepi.2017.11.005

Sabine, E. (1840). Contributions to terrestrial magnetism. No. i. *Philosophical Transactions of the Royal Society of London*.

Sabine, E. (1843). Contributions to terrestrial magnetism. No. v. *Philosophical Transactions of the Royal Society of London*.

Sabine, E. (1846). Contributions to terrestrial magnetism. No. viii. *Philosophical Transactions of the Royal Society of London*.

Sabine, E. (1849). Contributions to terrestrial magnetism. No. ix. *Philosophical Transactions of the Royal Society of London*.
Sabine, E. (1875). Contributions to terrestrial magnetism. No. xiv. *Philosophical Transactions of the Royal Society of London*, *165*, 161–203. https://doi.org/10.1098/rstl.1875.0004
Schnepp, E., Thallner, D., Arneitz, P., & Leonhardt, R. (2020). New archeomagnetic secular variation data from Central Europe, II: Intensities. *Physics of the Earth and Planetary Interiors*, *309*, 106605. https://doi.org/10.1016/j.pepi.2020.106605
Sternberg, R. S. (1989). Secular variation of archaeomagnetic direction in the American Southwest, AD 750–1425. *Journal of Geophysical Research*, *94*(B1), 527–546. https://doi.org/10.1029/jb094ib01p00527
Suttie, N., Holme, R., Hill, M. J., & Shaw, J. (2011). Consistent treatment of errors in archaeointensity implies rapid decay of the dipole prior to 1840. *Earth and Planetary Science Letters*, *304*(1–2), 13–21. https://doi.org/10.1016/j.epsl.2011.02.010
Tema, E. (2009). Estimate of the magnetic anisotropy effect on the archaeomagnetic inclination of ancient bricks. *Physics of the Earth and Planetary Interiors*, *176*(3–4), 213–223. https://doi.org/10.1016/j.pepi.2009.05.007
Terra-Nova, F., Amit, H., Hartmann, G. A., Trindade, R. I., & Pinheiro, K. J. (2017). Relating the South Atlantic Anomaly and geomagnetic flux patches. *Physics of the Earth and Planetary Interiors*, *266*, 39–53. https://doi.org/10.1016/j.pepi.2017.03.002
Thellier, E., & Thellier, O. (1959). Sur l'intensité du champ magnétique terrestre dans le passé historique et géologique. *Annales de Geophysique*, *15*, 285–337.
Troyano, M., Gallet, Y., Genevey, A., Pavlov, V., Fournier, A., Lagroix, F., et al. (2021). Analyzing the geomagnetic axial dipole field moment over the historical period from new archeointensity results at Bukhara (Uzbekistan, Central Asia). *Physics of the Earth and Planetary Interiors*, *310*, 106633. https://doi.org/10.1016/j.pepi.2020.106633
Turner, G. M., Kinger, R., McFadgen, B., & Gevers, M. (2020). The first archaeointensity records from New Zealand: Evidence for a fifteenth century AD archaeomagnetic 'spike' in the SW Pacific region? *Geological Society, London, Special Publications*, *497*(1), 47–72. https://doi.org/10.1144/sp497-2019-71
Unknown. (1684). *Log of Bristto prize. Manuscript, Sloane/854*. British Library.
Van Bemmelen, W. (1899). *Die Abweichung der Magnetnadel: Beobachtungen, Säcular-Variation, Wert-und Isogonensysteme bis zur Mitte des XVIIIten Jahrhunderts* (Vol. 21). Landsdrukkerij.
Veitch, R. J., Hedley, I. G., & Wagner, J.-J. (1984). An investigation of the intensity of the geomagnetic field during Roman times using magnetically anisotropic bricks and tiles. *Archives des Sciences*, *37*(3), 359–373.
Wicht, J., & Olson, P. (2004). A detailed study of the polarity reversal mechanism in a numerical dynamo model. *Geochemistry, Geophysics, Geosystems*, *5*(3). https://doi.org/10.1029/2003gc000602